This is the accepted manuscript made available via CHORUS. The article has been published as:

Inverse spin Hall effect in Au_{x}Ta_{1−x} alloy films

D. Qu, S. Y. Huang, G. Y. Guo, and C. L. Chien

Phys. Rev. B **97**, 024402 — Published 3 January 2018

DOI: 10.1103/PhysRevB.97.024402

Inverse spin Hall effect in Au_xTa_{1-x} alloy films

D. Qu[1], S. Y. Huang[2], G. Y. Guo[2,3], and C. L. Chien[1*]

[1]Department of Physics and Astronomy, Johns Hopkins University, Baltimore, Maryland 21218, USA

[2]Department of Physics, National Taiwan University, Taipei 10617, Taiwan

[3]Physics Division, National Center for Theoretical Sciences, Hsinchu 30013, Taiwan

Abstract

Gold (Au) and tantalum (Ta) metals are two important spin Hall materials with diametrically different crystalline structure, resistivity, and spin Hall angle. By vapor quenching, Au_xTa_{1-x} alloys of different crystalline and amorphous structures, stable and metastable, have been formed over the entire composition range. We have studied the inverse spin Hall voltage induced by the longitudinal spin Seebeck effect in Au_xTa_{1-x} alloy films. We have found that the inverse spin Hall voltage ΔV_{ISHE}, resistivity ρ, and the spin Hall angle θ_{SH} vary smoothly with composition. Both the spin Hall angle and the spin Hall conductivity exhibit a quasi-linear dependence on composition in the concentrated alloy regime, despite drastic differences in other properties. As corroborated by first-principle calculation, we show the contribution to spin Hall effect in Au_xTa_{1-x} alloy is dominated by the number of valence electrons. We also show that the magnetoresistance correlates with the spin Hall angle.

I. Introduction

Pure spin current has attracted a great deal of attention due to both scientific interest and technological importance. A pure spin current without a net charge current delivers angular momentum using a minimal of charge carriers hence dissipating much less heat. Extensive studies have been focused on the generation, the detection, and the utilization of pure spin current [1]. The spin Hall effect (SHE) and the inverse spin Hall effect (ISHE), the two reciprocal effects, are the key effects in generating and detecting pure spin current [2]. When a charge current $\boldsymbol{j_C}$ flows in a metal with strong spin-orbit coupling (SOC), the SHE generates a pure spin current $\boldsymbol{j_S} = \theta_{SH}(\hbar/2e)\,\boldsymbol{j_C}\times\boldsymbol{\sigma}$ in the lateral direction that gives rise to spin accumulation, where $\boldsymbol{\sigma}$ is the spin index, $\hbar$ is the reduced Planck constant, and e is the electronic charge. The spin Hall angle θ_{SH} measures the prowess of a material in converting charge current to spin current and vice versa. Materials with large θ_{SH} are essential for the next generation spintronic devices based on the pure spin current phenomena. Heavy *5d* metals with strong SOC, such as Pt (0.37% to 11%), W (-14% to -33%), Au (0.16% to 11.3%), Ta (-0.37% to -12%), etc., indeed have large values of θ_{SH} [1, 3-12]. However, within the *3d* metals, while some (e.g., Cu) have very small θ_{SH} (< 0.32%) [10], but others, notably Cr (-5%) [13, 14] and even ferromagnetic metals, such as permalloy (2% to 3%) [13, 15, 16], have unexpectedly large θ_{SH}, much larger than those accommodated by theoretical calculations for *3d* metals [17]. These results strongly suggest a more important role of *d*-orbital electrons in the SHE/ISHE comparing to the atomic number Z [13]. The significant role that *d*-orbital electrons play in the spin Hall effect has been appreciated in transition metals [3], where the strength of the spin-orbit coupling is found to be proportional to $\langle l\cdot s\rangle$. This principle

is also applicable to *f*-electron systems, where researchers have found that rare-earth elements near 1/4 and 3/4 *f*-orbital fillings (*e.g.* Ho) have stronger spin Hall effect than other *f*-electron elements [18].

The SHE in a non-magnetic metal is similar to the anomalous Hall effect (AHE) in a ferromagnetic metal [19]; both involving the separation of charge carriers with opposite spins. As such, the spin-dependent voltage induced by the AHE in various ferromagnetic metals and that by the SHE in metals can be of either sign. While there is no simple rule for the sign of AHE in ferromagnet, within the SHE/ISHE in the *5d* metals, one observes $\theta_{SH} < 0$ (e.g., W, Ta) and $\theta_{SH} > 0$ (e.g., Pt, Au) for those with less than and more than half full *5d* shell, respectively [3].

The AHE and SHE/ISHE have three main contributions of intrinsic deflection, skew scattering, and side jump [19]. The intrinsic contribution from the Berry curvature is intimately connected to the Fermi surface and the band structure of the material, whereas the skew scattering and the side jump are extrinsic mechanisms. Since the Berry curvature is very sensitive to changes in the Fermi surface, drastic modifications in the SHE/ISHE may be expected for different crystal structures. The side jump scattering contribution is usually the smallest among the three scattering mechanisms, but may dominate at high impurity concentrations. However, identifying the relative importance of the three contributions are far more difficult. In the case of the AHE in ferromagnets, clarification occurred only in recent years after decades of controversies.

The important role of intrinsic mechanism has been identified for metals with different crystal structures [5-7, 11] as well as anisotropies [20, 21]. For example, the θ_{SH} for β-W (-33%) [7] and β-Ta (-3% ~ -12%) [6, 11] are much larger than α-W (-7%) [7]

and α-Ta (-0.3%) [5]. The θ_{SH} for (001) oriented $IrMn_3$ (20%) is about two times larger than (111) oriented or polycrystalline $IrMn_3$ (10%) [21]. On the other hand, the importance of extrinsic scattering contribution has been mostly observed in doped metals, where large θ_{SH} are acquired through extrinsic resonant scattering by doping a small amount of alien atoms, for example Ir or Bi in the Cu host [22-24]; or W in the Au [25]. These special alloys of dilute heavy impurities in a noble metal with long mean free path accommodate multiple scattering events.

Most studies of the SHE/ISHE have been made in elemental metals or dilute alloys [22-26]. There are few studies of spin current and θ_{SH} in alloys through systematic variation of composition over the entire composition region [27, 28], and none crossing multiple distinct structures. In this work, we report on such studies in Au-Ta alloys over the entire composition range. We show experimentally that the spin Hall angle exhibit a quasi-linear dependence on composition despite drastic differences in other properties. Through first-principle calculations, we find the calculated configuration averaged spin Hall conductivity agrees qualitatively well with the experiment data, which increases monotonically with increasing Au concentration. The configuration averaged spin Hall conductivity depends strongly on the number of valence electrons over the crystalline structure. The consistency between the theoretical calculation and experimental results suggest the important role of valence electrons over crystallinity in alloys.

The Au-Ta alloys encompass large contrast in crystal structure, resistivity, and spin Hall angle. Pure Au has a face-centered cubic (fcc) structure, whereas Ta has a body-centered cubic (bcc α-phase)/tetragonal (β-phase) structure. In addition, amorphous Au-Ta alloys have also been realized in an extended composition range thus providing

still another structure variation. The electrical resistivity of Au is in the μΩ-cm range, typical of a good metal, whereas that of Ta, in the 300 μΩ-cm range, is at the other extreme. Equally striking is the fact that Au and Ta have a sizable spin Hall angle θ_{SH} but of opposite signs [3,5-6, 8-12]. Given the sharp contrast between Au and Ta, the investigation of pure spin current phenomena in Au-Ta alloys over the composition may provide important insight into the mechanisms of the SHE/ISHE.

Equilibrium phase diagram of Au-Ta alloys show limited solubility at the Au-rich (up to 30% Ta in Au) and Ta-rich ends (up to 20% Au in Ta) and some intermetallic compounds, including Au_2Ta_3 and $AuTa_5$ [29]. However, extensive studies have demonstrated that alloy compositions not accommodated by the equilibrium phase diagram can be readily obtained in vapor-deposited thin films [30, 31]. Sputtering is an effective vapor-quench method that can capture metastable crystalline and amorphous alloys as realized in the metastable Au-Ta alloys.

II. Experimental Method

We use co-sputtering from two sources of Au and Ta to form Au-Ta alloys. The substrate at room temperature is placed at a specific height (about 4 cm) above and in between the Au and the Ta sputtering sources, as shown in Fig. 1(a). We deposited thin films on Si and yttrium iron garnet (YIG) substrates. The sample on Si substrate (0.5 mm with 200 nm thermally oxidized SiO_2 layer) are cut into larger pieces (10 mm × 40 mm) for obtaining the deposition rates. With one obligue deposition source, a wedged film is obtained. By adjusting the substrate height and properly tilting the deposition source, the thickness in the wedged film can be made linearly varying with position. After a similar

procedure being applied to the other deposition source, we adjusted the deposition rates from the two sources to form Au-Ta alloys of approximately the same thickness with composition continuously varying and quasi-linearly along the wedged direction as shown in Fig. 1(a). The compositions for the ISHE measurements were also separately determined by x-ray photoelectron spectroscopy (XPS). On the other hand, the commercially obtained 0.5 mm thick polycrystalline YIG substrates are cut into smaller pieces (3 mm × 7 mm) for patterning into Hall bars for transport measurement. They are aligned in an array where the long edges are parallel with each other while perpendicular to the gun direction, as shown in Fig. 1(b).

X-ray diffraction (XRD) results for the 150-nm thick Au_xTa_{1-x} films on a continuous Si substrate are shown in Fig. 1(d). The Au-rich films are fcc (111)-textured same as that of Au, whereas the Ta-rich films have the same patterns as that of β-Ta. The slight shift of the diffraction peaks in both the Au-rich and the Ta-rich films is due to different metallic radii of 1.45 Å and 1.35 Å for Ta and Au respectively. However, for Au compositions roughly from 30% to 40%, very broad diffraction peaks instead of sharp diffraction peaks have been observed, indicating the formation of amorphous state. This behavior has been observed previously in many binary alloys, where the amorphous state is realized in the mid-composition range, determined by the size difference of the two elements [32, 33]. Therefore, in Au-Ta alloys, there are three distinct structures (fcc, amorphous, and β-Ta) to explore changes in the ISHE due to intrinsic scattering.

We employ the longitudinal spin Seebeck effect (LSSE) to thermally inject the pure spin current and measure ISHE in the Au_xTa_{1-x} films [34]. Thin films of about 5-nm thick are deposited onto 0.5-mm thick YIG substrates under room temperature. Before

deposition, YIG substrate is covered with photoresist except for a Hall bar area with dimensions of 4.5 mm × 0.2 mm for the long segment, and 2 mm × 0.2 mm for the short segments, as shown in Fig. 1(c). Through a lift-off procedure, the thin film is patterned into the Hall bar structure without any heat treatment. Under an out-of-plane temperature gradient of 20 K/mm, the pure spin current is injected from YIG into Au-Ta alloy via the LSSE. The ISHE voltage is detected along the long direction of the sample while the YIG magnetization direction, hence the spin index of the pure spin current, is aligned in the short direction by an external magnetic field.

III. Results and Discussion

A. Inverse spin Hall effect

Representative ISHE voltages due to the LSSE of the Au_xTa_{1-x} films as a function of the magnetic field are shown in Fig. 2(a). According to $V_{ISHE} \propto \sigma \times J_S$, the inverse spin Hall voltage is proportional to the cross product of the spin orientation σ, which is determined by the direction of the magnetization of YIG, and the spin current J_S. In Fig. 2(a), the ISHE of Au_xTa_{1-x} does not follow the magnetization curve of bulk YIG (inset of Fig 2(a)) at the low magnetic field. This is due to the non-collinear magnetization between surface and bulk YIG [35]. For each sample, the voltage difference between saturated positive and negative fields defines the ISHE magnitude ΔV_{ISHE} (which is twice the inverse spin Hall voltage V_{ISHE}). Since all the results are shown with the same scale, it is immediately clear that the value of V_{ISHE} changes continuously with composition and that the sign of V_{ISHE} in the Au-rich and the Ta-rich samples are opposite as shown in Fig. 2(a). The ISHE voltage (ΔV_{ISHE}) dependence on composition is plotted in Fig. 2(b). The

Ta-rich films have negative ΔV_{ISHE}, whose values changes sharply with composition. In contrast, the Au-rich films have positive ΔV_{ISHE}, whose value remains roughly the same as that of Au. Most notably, the value of ΔV_{ISHE} varies smoothly as the composition is systematically varied, notwithstanding the fact that there are three distinct structures in the Au-Ta alloys. These results have already shown that the interfaces of the Au-Ta alloys/YIG samples are highly consistent, which allow us to systematically study the variation of spin Hall angle and spin Hall conductivity on compositions.

From earlier studies [9] we show that the measured $\Delta V_{ISHE}(t)$ for a thin film of thickness t can be expressed as

$$\Delta V_{ISHE}(t) = 2CL\nabla T\rho(t)\theta_{SH}\frac{\lambda_{sd}}{t}\tanh(\frac{t}{2\lambda_{sd}}) \qquad (1)$$

where L = 4 mm is the sample length, ∇T=*20 K/mm* is the temperature gradient, λ_{sd} is the spin diffusion length, and C is the spin current injection coefficient. Of all the factors, other than the spin Hall angle θ_{SH}, which we wish to determine, the resistivity $\rho(t)$ has the strongest variation and must be measured [9, 36]. The results of the resistivity of the samples of Au_xTa_{1-x}/YIG are shown in Fig. 2(c). As expected, Ta-rich films have up to 30 times larger resistivity than those of the Au-rich films, thus carrying the overwhelming variation of ΔV_{ISHE}. The amorphous alloys, well known for its high resistivity, have values slightly higher than those of the Ta-rich crystalline alloys. It is noted in Fig. 2(c) that the resistivity likewise changes smoothly with composition without discernable changes across phase boundaries. From the measured ΔV_{ISHE} and $\rho(t)$, which are smoothly varying with the composition, the remaining factors, including spin mixing conductance and spin diffusion length, in Eq. (1) must vary smoothly likewise.

The factor $C = \frac{2e}{\hbar}\frac{\gamma\hbar\rho' k_m^3 l_m}{4\pi M\pi^2}\frac{B_1 B_S}{B_2} g_{eff}^{\uparrow\downarrow} k_B$ in Eq. (1) is the spin current injection coefficient, containing the magnetic properties of YIG (saturation magnetization $4\pi M$=140 kA/m, gyromagnetic ratio γ=1.76×10^{11} s^{-1}T^{-1}, magnon diffusion length l_m=70 nm, finite ferromagnetic insulator thickness factor ρ'~1, maximum wave number k_m=2×10^9 m^{-1}, parameters from diffusion equation B_1=0.55, B_s=2.2×10^{-4}, B_2=5.1×10^{-3}, the Planck constant $\hbar$=1.054×10^{-34} J·s, the electron charge e=1.6×10^{-19} C, the Boltzmann constant k_B=1.38×10^{-23} J·K^{-1}) [37] and the spin mixing conductance ($g_{eff}^{\uparrow\downarrow}$), the interfacial momentum transfer efficiency, between the metal layer and YIG. Although there are different reported values of spin-mixing conductance for Au and Ta on YIG [38-40], they only differ by about a factor of two from one systematic determination ($g_{eff}^{\uparrow\downarrow}(Au) = 2.7 \times 10^{18}\ m^{-2}, g_{eff}^{\uparrow\downarrow}(Ta) = 5.4 \times 10^{18}\ m^{-2}$) [10]. Therefore, the spin injection coefficients C of Au and Ta on YIG differ by about a factor of two, with Ta higher than Au. The spin diffusion length λ_{SF} obtained from the thickness dependent measurement for Au and Ta on YIG is about 10 nm and 2 nm, respectively [9]. The short λ_{SF} for Au on YIG is possibly limited by impedance mismatch at metal/insulator interface and inherent to perpendicular transport. For the t = 5 nm thick alloy film, we have the factor of $\left[\left(\frac{\lambda_{SF}}{t}\right) tanh\left(\frac{t}{2\lambda_{SF}}\right)\right]$ of 0.49 and 0.34 for Au and Ta, respectively. To further simplify Eq.(1), we rewrite the equation as

$$\Delta V_{ISHE} \approx D\rho(t)\theta_{SH}, \qquad (2)$$

where $D = [2L\nabla T]C\left[\left(\frac{\lambda_{SF}}{t}\right) tanh\left(\frac{t}{2\lambda_{SF}}\right)\right]$. Considering the small variation in C and $\left[\left(\frac{\lambda_{SF}}{t}\right) tanh\left(\frac{t}{2\lambda_{SF}}\right)\right]$, the difference of D between Au and Ta is essentially within a factor

of 1.5, far smaller than the variation of ΔV_{ISHE} and $\rho(t)$. As reported recently, the spin current from YIG can be robustly and reliably generated by the SSE. [41]. We therefore use the approximation $D \approx 200\ Am^{-1}$, estimated from the above mentioned quantities, as the proportional constant. Thus, the θ_{SH} can be approximated by $(1/D)\Delta V_{ISHE}/\rho(t)$. However, when analysing the data, we used the full expression Eq.(1).

The variation of θ_{SH} on composition is revealed by $\Delta V_{ISHE}/\rho(t)$, which is shown in Fig. 3(a). Remarkably, this variation is monotonic, approximately linear. Based on the above analysis, we estimate the θ_{SH} values for pure Au ($\theta_{Au}=1.4\%$) and pure Ta ($\theta_{Ta}=-1.0\%$). These values fall in the broad range of the θ_{SH} reported previously, Au (0.16% to 11.3%) and Ta (-0.37% to -12%) [1, 9, 12]. Essentially all values of θ_{SH} except that of Au are nearly on a linear relationship with composition. Consider the drastic differences among the three structures of fcc, amorphous, and β-Ta, the linear behavior of the θ_{SH} over essentially the entire composition range is indeed remarkable. We can also approximate the spin Hall conductivity (SHC) $\sigma_{SH} = \theta_{SH}/\rho_{xx}$ in these films by dividing the spin Hall angle by resistivity ρ_{xx}. As shown in Fig. 3(b), we find σ_{SH} also varies quasi-linearly at most composition except increasing more rapidly at the Au end.

B. First-principle calculation

To help understand the experimental results, we have performed first-principles calculations (Appendix) of the electronic band structure and SHC of Au-Ta alloys in the Ta-rich β-structure and Au-rich fcc structure as well as pure fcc Au, pure α- and β-phase Ta metals. The calculated SHC as a function of Au composition (x) are shown in Fig. 4. Results of individual compositions are shown as circles, diamonds, and triangles. Starting

with a negative value [-378 (ħ/e) (S/cm)] of pure β–Ta, the SHC remains more or less unchanged in the β–phase over an extended composition range. However, when entering the fcc phase, the SHC increases steadily with x and changes sign at about x = ~65 %. At higher x, the SHC increases rather sharply until x = ~97 % where the SHC reaches the maximum of about 1016 (ħ/e) (S/cm), and then reduces to that of pure fcc Au [446 (ħ/e) (S/cm)]. This peak is due to the skew scattering in Au rich films. To confirm this, we further estimate the skew scattering contribution (Appendix), and subtract it from the total SHC (red up triangles). The resultant "intrinsic" SHC are plotted as blue down triangles. The "intrinsic" SHC (blue) is much smoother comparing with the total SHC (red) suggesting the importance of extrinsic scattering in Au rich films.

We note that the measured SHC [Fig. 3(b)] is much smaller than the calculated SHC (Fig. 4). This is possibly due to the loss of spin current across the metal/YIG interface. Nevertheless, they agree qualitatively well with each other, both increasing monotonically x increases. We also note the peak in calculated SHC (Fig. 4) as described previously is not observed when in the measured SHC [Fig. 3(b)]. One possibility is the reduction of extrinsic scattering at room temperature (the calculated SHC is at near zero temperature). Another possibility is the enhanced measured SHC in thin Au film caused by extrinsic scattering from suface scattering. Regardless of the last point, we have shown that both experimentally and theoretically, the spin Hall conductivity vary monotonically across the atomic concentration, which is highly unexpected for materials with sharp transitions in crystalline structure.

We also note that the β–structure is tetragonal and thus anisotropic. The calculated SHC of σ_{sH}^{xy} and σ_{sH}^{xz} (σ_{sH}^{yz}) are -500 and -309 (ħ/e) (S/cm), respectively and

indeed anisotropic. The average value is plotted in Fig. 4, since thin films are polycrystalline. For comparison, the calculated SHC for pure bcc Ta is -103 (ħ/e) (S/cm) (see also Fig. 4). This suggests that the measured SHC of pure Ta would depend significantly on the orientation and structure of the samples used in different measurements [5, 6]. Similar anisotropic dependence of SHC has also been reported previously [20, 21].

The SHCs calculated as a function of the number of valence electrons for pure bcc Ta and fcc Au (Appendix) within the rigid band approximation are also displayed as solid or dashed lines in Fig. 4. We note that the SHC calculated using the rigid band model agree with the measured SHC in sign, viz, they are negative in the β–phase and become positive in the fcc structure. However, they do not vary monotonically with Au concentration. The configuration averaged SHC (circles, diamonds, and triangles) contains, in principle, all the extrinsic skew-scattering and side-jump as well as intrinsic contributions to the SHC, if a sufficiently large supercell is used and a large number of configurations are sampled. Consequently, the SHC would not depend strongly on the crystal structure but rather would be determined mainly by the number of valence electrons. This explains that the SHC varies nearly monotonically as the Au concentration increases, being in semi-quantitative agreement with the measured SHC shown in Fig. 3(b). As an example that the SHC calculated here contains both extrinsic and intrinsic contribution, we note that the SHC calculated using a 3×3×3 supercell of $Cu_{31}Bi$ (Bi at 0.926 %) is ~5555 (ħ/e) (S/cm), being in good agreement with the measurement on dilute Bi in Cu [23] and also explicit *ab initio* skew-scattering calculation based on the Boltzmann transport theory [24]. That the calculated SHC

changes sign at much larger Au concentration could be attributed to a too small supercell (4 atoms simple cubic cell) used here.

C. Magnetoresistance

In addition to the ISHE in the alloy films, we have also measured the magnetoresistance (MR) of the Au-Ta alloy films on YIG with magnetic field in plane, both parallel ($\rho_{||}$) and transverse (ρ_{Γ}) to the electric current direction, and with field perpendicular to the film plane ($\rho_{\perp}$). An unusual MR with the unique characteristics of $\rho_{\perp} \approx \rho_{||} > \rho_{\Gamma}$ (rather different from the well-known AMR of $\rho_{||} > \rho_{\Gamma} \approx \rho_{\perp}$) has been observed in HM/YIG, where HM is Pt, Au, Ta, W etc. [42-44]. Pure Ta has a sizable MR ratio of $\Delta\rho/\rho_{||}$ of 2×10^{-5}, while that for Au is more than one order of magnitude smaller as known previously [8, 9]. The small MR in the Au side is mainly due to its low resistance, long spin diffusion length, and the lack of magnetic proximity effect. Interestingly, the MR ratios for the alloy films do not show a linear dependence on the alloy composition as shown in Fig. 5. Instead, the MR ratio at the Ta rich side decreases rapidly and becomes negligible at x$\approx$40%, where the θ_{SH} of the alloy crosses *zero*. We have earlier reported zero MR in metal on YIG with altered surface due to the blockage of spin current. The MR in the HM/YIG system have two contributions: the spin current at low magnetic field (H<1000 Oe), which can be explained by the spin Hall MR model [45]; and the magnetic proximity effect at high magnetic field (H> 10 kOe) [46]. Therefore, in the Au-Ta system on the untreated YIG substrate, the near zero MR under the low magnetic field regime is the result of a lack of spin current generation and conversion, as

represented by the nearly zero $\theta_{SH,}$ of the material. Similar behavior has also been demonstrated in the Pt-Ta system [47].

IV. Conclusion

As we have shown in this work, we studied the inverse spin Hall effect in Au-Ta alloys. Au and Ta are materials with diametrically different physical properties in crystalline structure, resistivity, and, most importantly, they have opposite sign of the spin Hall angle. We captured the metastable crystalline or amorphous Au-Ta alloy thin films, that are absent in the equilibrium phase diagram, by vapor-quenching via co-sputtering. Despite the three distinct structures of bcc, amorphous, and β-Ta, both the θ_{SH} and σ_{SH} of the Au-Ta alloy film in the concentrated regime depend *monotonically* on the Au and Ta compositions and cross the zero value smoothly. Our first-principle calculation on the configuration averaged σ_{SH} also agrees qualitatively well with the experimental result, suggesting the vital role of the valence electrons instead of crystallinity in contributing to the spin Hall effect in alloy films. Knowing the significant role *d* electrons play in spin Hall effect is crucial in understanding the large spin Hall angle in some *3d* metals, and moreover, as we have demonstrated in this work, it provides guidance in constructing materials with the designated value of spin Hall angle for future spintronic devices.

Acknowledgement

We thank Steven Tran and Tsao-Chi Chuang for the help of sample characterization. This work was supported by the U.S. Department of Energy, Office of

Science, Basic Energy Science, under Award Grant No. DE-SC0009390. D.Q. was supported in part by SHINES, an EFRC funded by the US DOE Basic Energy Science under Award No. SC0012670. S. Y. H acknowledged the Golden Jade Fellowship of the Kenda Foundation, Taiwan. This work was also partially supported by the Ministry of Science and Technology of Taiwan, under the Grant Nos. MOST 103-2212-M-002-021-MY3 and MOST 104-2112-M-002-002-MY3, as well as Academia Sinica and Kenda Foundation, Taiwan.

Appendix

The first-principles calculations of spin Hall conductivity (SHC) are based on the density functional theory (DFT) with the generalized gradient approximation (GGA) [48]. The accurate projector-augmented wave method [49], as implemented in the VASP package [50, 51] is used. Experimental lattice constants for pure fcc Au (a = 4.08 Å) and β-Ta (a = 10.194 Å, c = 5.313 Å) [52] are used for Au-rich fcc alloys and Ta-rich β-phase alloys, respectively. Calculated SHCs for individual compositions are shown in Fig. 4 as circles, diamonds, and triangles. Experimental lattice constant (a = 3.30 Å) is used for bcc Ta. For Au-rich fcc alloys ($Ta_{1-x}Au_x$), we consider individual Au compositions of x = 1/2, 3/4, 28/32, 30/32, and 31/32. For x = 1/2 and 3/4, a simple cubic supercell with 4 atoms per unit cell is used, while for x = 28/32, 30/32 and 31/32, a 2×2×2 simple cubic supercell with 32 atoms per unit cell is used. For Ta-rich β–phase alloys, we consider Au composition x = 2/30, 4/30, and 8/30 in the primitive unit cell of pure β–Ta structure. For each composition, a number of configurations were generated and their atomic positions were relaxed theoretically within the DFT-GGA with the lattice constants fixed. A few

low energy configurations were selected and their SHC (σ_{sH}) were calculated. The SHC for each structure is calculated as an integral of spin Berry curvature on all occupied bands over the Brillouin zone [4, 53]. The final SHC for each composition is given by the configuration average of SHC, i.e.,

$$\sigma_{sH} = \left[\sum_{i=1}^{N} \sigma_{sH}^{(i)} \exp(\Delta E_i / k_B T)\right] / \left[\sum_{i=1}^{N} \exp(\Delta E_i / k_B T)\right]$$

where N is the number of configurations and ΔE_i is the energy of the i^{th} configuration relative to the lowest configuration energy. For each structure, a sufficiently dense **k**-point mesh is used for Brillouin zone integration by the tetrahedron method such that the calculated SHC converges within a few percent.

Figure 4 shows that the calculated SHC increases sharply as the Ta composition decreases in the Au-rich region, indicating a significant contribution due to the extrinsic skew-scattering (SK) of Ta impurities. To quantify the SK contribution, we estimate the skew-scattering by taking the difference in the calculated SHC between pure Au and 96.875 % Au. Using this estimated SHC due to the SK and together with the experimental residual resistivity for Au-Ta alloys reported in [54], we estimate the skew-scattering spin Hall angle (SHA) which should be constant in the dilute Ta impurity region. We then use this SHA together with the longitudinal conductivities measured here to obtain the estimated SHC due to the SK in the Au-rich region. The calculated total SHC subtracted of the estimated skew-scattering SHC are shown in Fig. 4 as blue down triangles (or fcc-"intrinsic"). It is clear that the fcc-"intrinsic" SHC curve (blue down triangles) is much smoother in the small Ta concentration region than the calculated total SHC curve (red up triangles).

Finally, we show the calculated band structures and also SHC as a function of the Fermi level for bcc Ta (Fig. 6) and fcc Au (Fig. 7). The band structure and SHC of fcc Au are very similar to that reported previously in [55] calculated using a different band structure method (i.e., linear muffin-tin orbital method with the atomic sphere approximation). In [3], the SHCs for entire 4*d* and 5*d* transition metal series have been calculated within the Kubo-Středa formalism using the tight-binding band structures fitted to the *ab initio* band structures. The tight-binding band structures of Au and Ta reported in [3] are similar to the corresponding band structures presented here (Figs. 6 and 7). Furthermore, the impurity scattering was taken into account by including a quasiparticle damping rate (γ), and thus the SHCs for pure Au and Ta presented here should be compared with those obtained with the smallest γ value in [3]. First of all, the SHCs reported in [3] and here agree in sign, i.e., the SHC for Au is positive and for Ta is negative. The SHC for Ta at γ = 0.002 (estimated from Fig. 8(b) in [3]) is -130 (ħ/e)(S/cm), being close to -103 (ħ/e)(S/cm) obtained here for bcc Ta. However, the SHC value of 114 (ħ/e)(S/cm) for Au at γ = 0.002 (estimated from Fig. 5(a) in [3]) is significantly smaller than 446 (ħ/e)(S/cm) for pure fcc Au reported here. The discrepancies could be attributed to the differences in the way the spin-orbit coupling (SOC) is treated since the SOC plays an important role in determining the SHC. In [3], the SOC is taken into account by a single SOC parameter (λ) of 0.03 Ry (0.013 Ry) for the *d*-orbitals for the entire 5*d* (4*d*) transition metal series, with the SOC for the *p*-orbitals being ignored. In the present calculations, the SOC strength is determined from the self-consistent potentials. The λ determined here for bcc Ta is 0.14 eV for the 5*d*-orbitals and 0.94 eV for 6*p*-orbitals, and for fcc Au, is 0.32 eV for the 5*d*-orbitals and 0.83 eV for 6*p*-

orbitals. We note that in fcc Au, the 5*d*-bands are completely filled and the conduction bands are of 6s6p characters. This suggests that the much smaller SHC value for Au reported in [3] could result from the neglecting of the SOC for the 6*p*-orbitals. Indeed, a recent calculation of the SHC for pure Au also within the Kubo-Středa formalism but using first-principles Korringa-Kohn-Rostoker multiple-scattering method [56] gives rise to a SHC value of 370 (ħ/e)(S/cm), which agrees quite well with 446 (ħ/e)(S/cm) reported here, but is significantly larger than 114 (ħ/e)(S/cm) reported in [3].

Recently, the ISHE of the dilute AuTa (up to 10% Ta doping) and AuW (up to 30% W doping) alloys are systematically studied through spin-current injection from Py [26]. The side-jump scattering is suggested to dominate in the dilute AuTa alloy, while the intrinsic mechanism is considered to be the main contribution to the dilute AuW alloy. In our work, through the spin-wave spin current from YIG we show that despite the very distinct physical property for pure Au and Ta, we observe a quasi-linear behavior of the ISHE signal from positive to negative over the entire composition, indicating the importance of the number of valence electrons.

*clchien@jhu.edu

References

1. J. Sinova, S. O. Valenzuela, J. Wunderlich, C. H. Back, and T. Jungwirth, Rev. Mod. Phys. **87**, 1213 (2015)

2. J. E. Hirsch, Phys. Rev. Lett. **83**, 1834 (1999)

3. T. Tanaka, H. Kontani, M. Naito, T. Naito, D. S. Hirashima, K. Yamada, and J. Inoue, Phys. Rev. B **77**, 165117 (2008)

4. G. Y. Guo, S. Murakami, T.-W. Chen and N. Nagaosa, Phys. Rev. Lett. **100**, 096401 (2008)

5. M. Morota, Y. Niimi, K. Ohnishi, D. H. Wei, T. Tanaka, H. Kontani, T. Kimura, and Y. Otani, Phys. Rev. B **83**, 174405 (2011)

6. L. Liu, C. F. Pai, Y. Li, H. W. Tseng, D. C. Ralph, and R. A. Buhrman, Science, **336**, 555 (2012)

7. C. F. Pai, L. Liu, Y. Li, H. W. Tseng, D. C. Ralph, and R. A. Buhrman, Appl. Phys. Lett. **101**, 124404 (2012)

8. D. Qu, S. Y. Huang, J. Hu, R. Wu, and C. L. Chien, Phys. Rev. Lett. **110**, 067206 (2013)

9. D. Qu, S. Y. Huang, B. F. Miao, S. X. Huang, and C. L. Chien, Phys. Rev. B **89**, 140407 (R) (2014)

10. H. L. Wang, C. H. Du, Y. Pu, R. Adur, P. C. Hammel, and F. Y. Yang, Phys. Rev. Lett. **112**, 197201 (2014)

11. J. E. Gomez, B. Zerai Tedlla, N. R. Alvarez, G. Alejandro, E. Goovaerts, and A. Butera, Phys. Rev. B **90**, 184401 (2014)

12. A. Hoffman, IEEE Trans. Magn **49,** 5172 (2013)

13. C. Du, H. Wang, F. Yang, and P. C. Hammel, Phys. Rev. B **90**, 140407(R) (2014)

14. D. Qu, S. Y. Huang, and C. L. Chien, Phys. Rev. B **92**, 020418 (R) (2015)

15. B. F. Miao, S. Y. Huang, D. Qu and C. L. Chien, Phys. Rev. Lett. **111**, 066602 (2013)

16. D. Tian, Y.-f. Li, D. Qu, X.-f. Jin and C. L. Chien, Appl. Phys. Lett. **106**, 212407 (2015)

17. F. Freimuth, S. Blugel, and Y. Mokrousov, Phys. Rev. Lett. **105**, 246602 (2010)

18. N. Reynolds, P. Jadaun, J. T. Heron, C. L. Jermain, J. Gibbons, R. Collette, R. A. Buhrman, D. G. Schlom, and D. C. Ralph, Phys. Rev. B **95**, 064412 (2017)

19. N. Nagaosa, J. Sinova, S. Onoda, A. H. MacDonald, and N. P. Ong, Rev. Mod. Phys. **82**, 1539 (2010)

20. W. Zhang, M. B. Jungfleisch, W. Jiang, J. E. Pearson, A. Hoffmann, F. Freimuth, and Y. Mokrousov, Phys. Rev. Lett. 113, 196602 (2014)

21. W. Zhang, W. Han, S.-Y. Yang, Y. Sun, Y. Zhang, B. Yan and S. S. P. Parkin, Sci. Adv. **2**, e1600759 (2016)

22. Y. Niimi, M. Morota, D. H. Wei, C. Deranlot, M. Basletic, A. Hamzic, A. Fert, and Y. Otani, Phys. Rev. Lett. **106**, 126601 (2011)

23. Y. Niimi, Y. Kawanishi, D. H. Wei, C. Deranlot, H. X. Yang, M. Chshiev, T. Valet, A. Fert, and Y. Otani, Phys. Rev. Lett. **109**, 156602 (2012)

24. M. Gradhand, D. V. Fedorov, P. Zahn, and Ingrid Mertig, Phys. Rev. B **81**, 245109 (2010).

25. P. Laczkowski, J. C. Rojas-Sanchez, W. Savero-Torres, H. Jaffres, N. Reyren, C. Deranlot, L. Notin, C. Beigne, A. Marty, J. P. Attane, L. Vila, J. M. George, and A. Fert, Appl. Phys. Lett. **104**, 142403 (2014)

26. P. Laczkowski, Y. Fu, H. Yang, J.-C. Rojas-Sánchez, P. Noel, V. T. Pham, G. Zahnd, C. Deranlot, S. Collin, C. Bouard, P. Warin, V. Maurel, M. Chshiev, A. Marty, J.-P. Attané, A. Fert, H. Jaffrès, L. Vila, and J.-M. George, Phys. Rev. B **96**, 140405(R) (2017)

27. L. K. Zou, S. H. Wang, Y. Zhang, J. R. Sun, J. W. Cai and S. S. Kang, Phys. Rev. B **93**, 014422 (2016)

28. M. Obstbaum, M. Decker, A. K. Greitner, M. Haertinger, T. N. G. Meier, M. Kronseder, K. Chadova, S. Wimmer, D. Kodderitzsch, H. Ebert, and C. H. Back, Phys. Rev. Lett. **117**, 167204 (2016)

29. W. G. Moffatt, "The Handbook of Binary Phase Diagrams" (Genium Pub. Corp, Amsterdam, 1981)

30. J. Q. Xiao, J. S. Jiang, and C. L. Chien, Phys. Rev. Lett. **68**, 3749 (1992)

31. J. R. Childress, and C. L. Chien, Phys. Rev. B **43**, 8089 (1991)

32. F. E. Luborsky, "Amorphous Metallic Alloys" (Butterworth & Co Ltd., London, 1983)

33. S. H. Liou and C. L. Chien, Phys. Rev. B **35**, 2443 (1987).

34. K. Uchida, H. Adachi, T. Ota, H. Nakayama, S. Maekawa, and E. Saitoh, Appl. Phys. Lett. **97**, 172505 (2010)

35. P.-H. Wu, and S.-Y. Huang, Phys. Rev. B **94**, 024405 (2016)

36. K. Fujiwara, Y. Fukuma, J. Matsuno, H. Idzuchi, Y. Niimi, Y. Otani and H. Takagi, Nat. Comm. **4**, 2893 (2013)

37. S. M. Rezende, R. L. Rodríguez-Suárez, R. O. Cunha, A. R. Rodrigues, F. L. A. Machado, G. A. Fonseca Guerra, J. C. Lopez Ortiz, and A. Azevedo, Phys. Rev. B **89**, 014416 (2014)

38. B. Heinrich, C. Burrowes, E. Montoya, B. Kardasz, E. Girt, Y.-Y. Song, Y. Sun, and M. Wu, Phys. Rev. Lett. **107**, 066604 (2011)

39. C. Burrowes, B. Heinrich, B. Kardasz, E. A. Montoya, E. Girt, Y. Sun, Y.-Y. Song, and M. Wu, Appl. Phys. Lett. **100**, 092403 (2012)

40. C. Hahn, G. de Loubens, O. Klein, M. Viret, V. V. Naletov, and J. Ben Youssef, Phys. Rev. B **87**, 174417 (2013)

41. F. J. Chang, J. G. Lin, and S. Y. Huang, Phys. Rev. Materials **1**, 031401(R) (2017)

42. S. Y. Huang, X. Fan, D. Qu, Y. P. Chen, W. G. Wang, J. Wu, T. Y. Chen, J. Q. Xiao, and C. L. Chien, Phys. Rev. Lett. 109, 107204 (2012)

43. H. Nakayama, M. Althammer, Y.-T Chen, K. Uchida, Y. Kajiwara, D. Kikuchi, T. Ohtani, S. Geprags, M. Opel, S. Takahashi, R. Gross, G. E. W. Bauer, S. T. B. Goennenwein, and E. Saitoh, Phys. Rev. Lett. **110**, 206601 (2013)

44. Y. -T Chen, S. Takahashi, H. Nakayama, M. Althammer, S. T. B. Goennenwein, E. Saitoh, and G. E. W. Bauer, Phys. Rev. B **87**, 144411 (2013)

45. Geprägs, M. Opel, S. Takahashi, R. Gross, G. E. W. Bauer, S. T. B. Goennenwein, and E. Saitoh, Phys. Rev. Lett. **110**, 206601 (2013)

46. B. F. Miao, S. Y. Huang, D. Qu, and C. L. Chien, Phys. Rev. Lett. **112**, 236601 (2014)

47. B. F. Miao, L. Sun, D. Wu, C. L. Chien, and H. F. Ding, Phys. Rev. B 94, 174430 (2016)

48. J. P. Perdew, K. Burke and M. Ernzerhof, Phys. Rev. Lett. **77**, 3865 (1996)

49. P. E. Blöchl, Phys. Rev. B **50**, 17953 (1994)

50. G. Kresse and J. Hafner, Phys. Rev. B **47**, 558 (1993)

51. G. Kresse and J. Furthmüller, Comput. Mat. Sci. **6**, 15 (1996)

52. P. T. Moseley and C. J. Seabrook, Acta Cryst. B **29**, 1170 (1973)

53. G. Y. Guo, Q. Niu and N. Nagaosa, Phys. Rev. B **89**, 214406 (2014)

54. T. Toyoda and K. Kume, J. Phys. F: Metal Phys. **5**, L134 (1975)

55. G. Y. Guo, J. Appl. Phys. **105**, 07C701 (2009)

56. K. Chadova, D. V. Fedorov, C. Herschbach, M. Gradhand, I. Mertig, D. Ködderitzsch, and H. Ebert, Phys. Rev. B **92**, 045120 (2015)

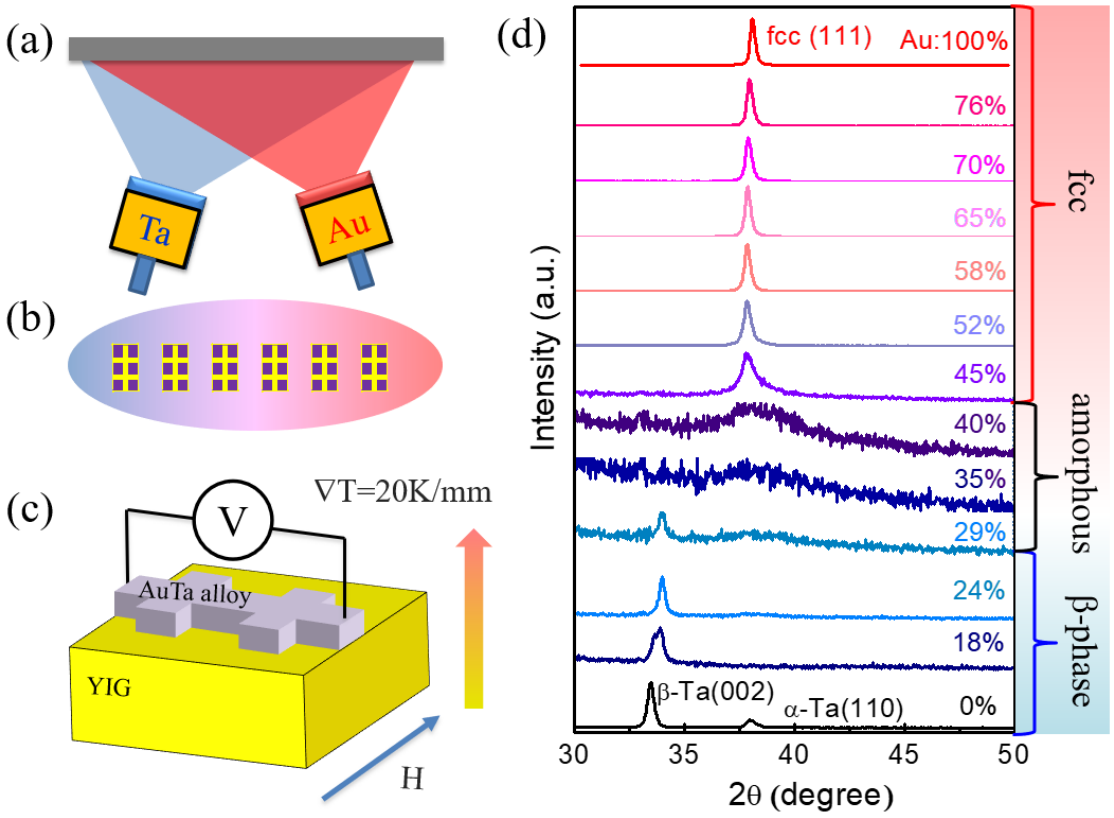

Fig. 1 (a) Side view of the co-deposition on Si substrate placed between the Ta and Au guns. (b) Top view of the YIG substrates array covered with inverted Hall bar photoresist. (c) Patterned Hall bar structures on YIG (aligned by a magnetic field) for spin injection by a vertical temperature gradient and measurements by inverse spin Hall effect. (c) X-ray diffraction pattern of the 150-nm Au_xTa_{1-x} samples with x from 0 to 1, showing structure of β-Ta, amorphous, and face centered cubic.

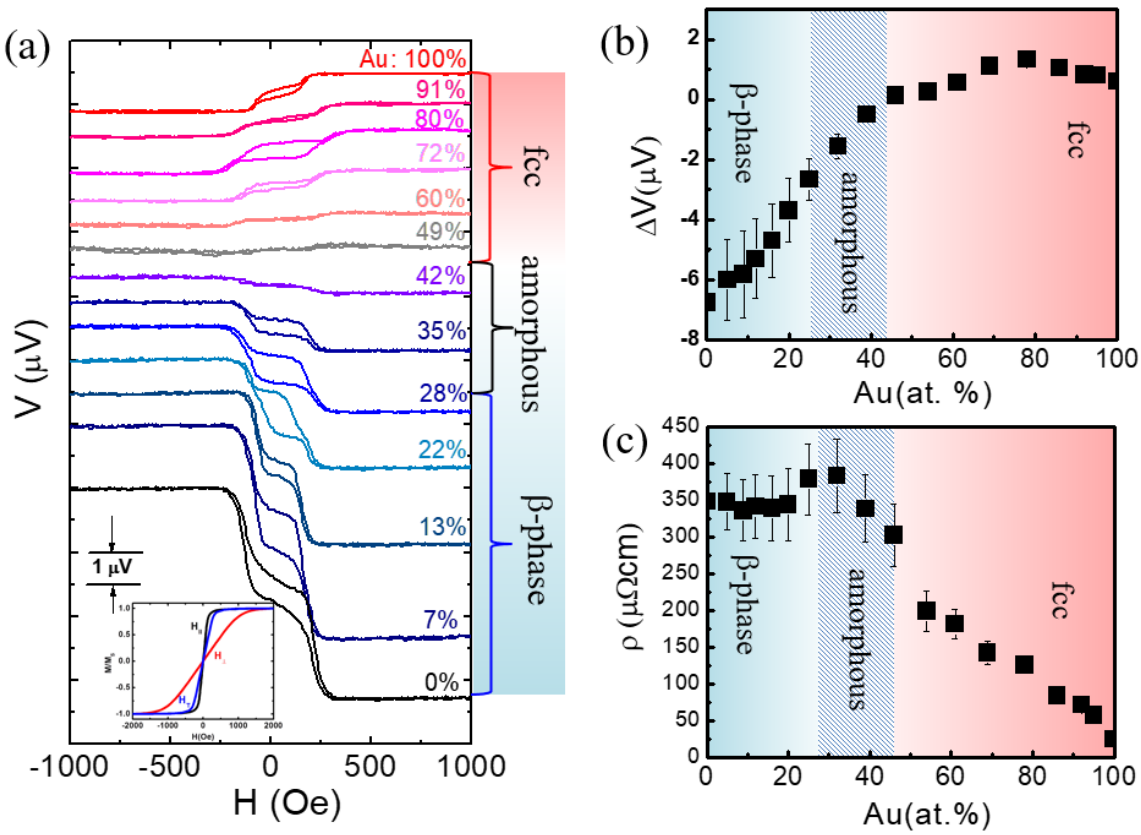

Fig. 2 (a) Inverse spin Hall voltage of Au_xTa_{1-x} alloy thin films under a vertical temperature gradient of 20 K/mm on samples 4 mm in length and 5 nm in thickness, and with an in-plane magnetic field from -1000 Oe to 1000 Oe. Inset is the M-H hysteresis for rectangular shaped YIG bulk substrate. Red, black and blue curves represent the magnetization obtained with field applied out-of-plane, inplane along long edge and inplane along short edge, respectively. The saturation Magnetization for bulk YIG is 1.8 kG, and the saturation magnetic field for in-plane and out-of-plane configurations are about 250 Oe and 1.8 kOe respectively. (b) Inverse spin Hall voltage and (c) resistivity of Au_xTa_{1-x} alloy thin films with x from 0 to 1.

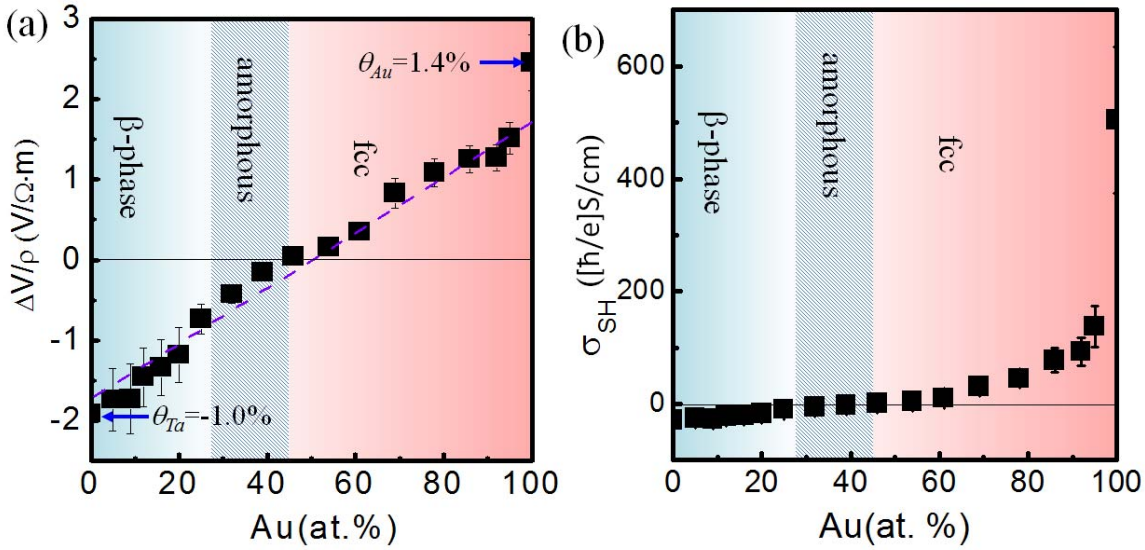

Fig. 3 (a) Plot of $\Delta V/\rho$ of Au_xTa_{1-x} alloy thin films as a function of composition. The spin Hall angle θ_{SH} of pure Au and pure Ta are marked at the two ends of the figure. Dashed line is a guide to the eyes. (b) Plot of spin Hall conductivity σ_{SH} vs. compositions.

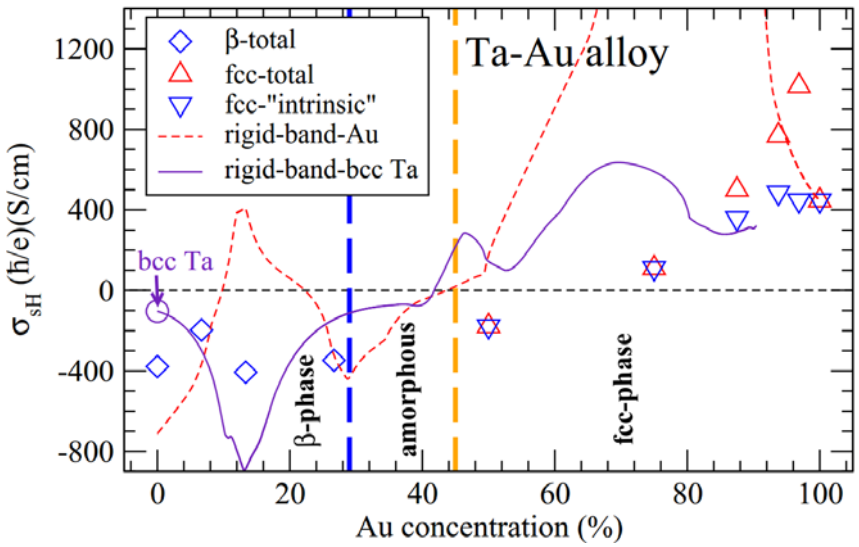

Fig. 4 Calculated SHC (σ_{SH}) vs. Au composition of Au_xTa_{1-x}. For comparison, the SHC derived from pure β–phase Ta and fcc Au within the rigid band model are also plotted as red dashed and indigo solid curves, respectively. The indigo circle at $x = 0$ indicates the SHC of pure bcc Ta. The calculated SHC (fcc-total, red up triangles) subtracted of the estimated skew-scattering contribution (Appendix) in the fcc phase are also displayed (fcc- "intrinsic", blue down triangles). The dashed blue and yellow vertical lines indicate, respectively, the boundaries between β–phase and amorphous phase as well as between amorphous phase and fcc-phase.

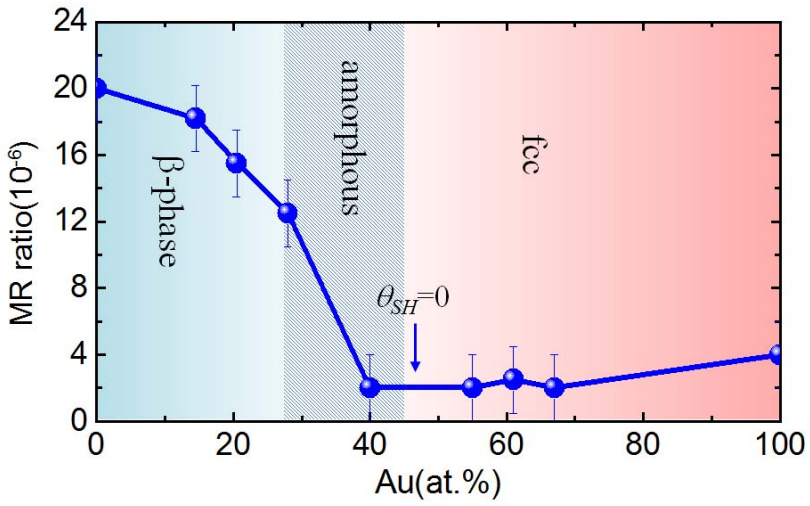

Fig. 5 (color online) Magnetoresistance ratio vs. compositions of Au_xTa_{1-x} alloy thin films. The MR vanishes at near x=40% where the spin Hall angle θ_{SH} also crosses 0. Solid line is a guide to the eyes.

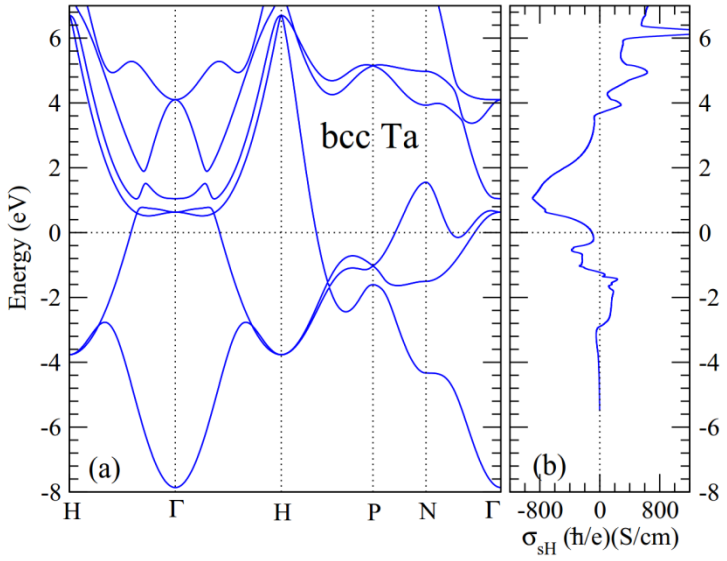

Fig. 6 (a) Relativistic band structure and SHC (σ_{sH}) of bcc Ta. The zero energy and dotted horizontal line is the Fermi level.

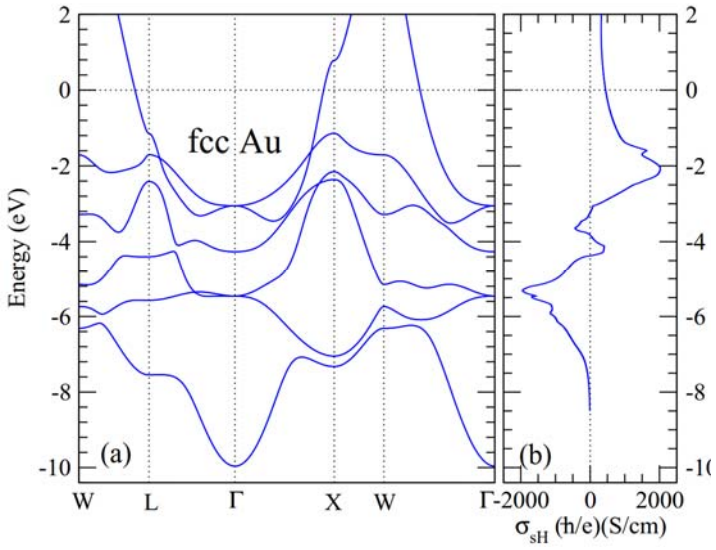

Fig. 7 (a) Relativistic band structure and SHC (σ_{sH}) of fcc Au. The zero energy and dotted horizontal line is the Fermi level.